

1 **Analysis of insoluble particles in hailstones in China**

2 Haifan Zhang¹, Xiangyu Lin¹, Qinghong Zhang^{1*}, Kai Bi^{2*}, Chan-Pang Ng¹, Yangze Ren¹, Huiwen Xue¹, Li Chen³, Zhuolin
3 Chang⁴

4 ¹Department of Atmospheric and Oceanic Sciences, School of Physics, Peking University, Beijing 100871, China

5 ²Field Experiment Base of Cloud and Precipitation Research in North China, China Meteorological Administration, Beijing
6 101200, China

7 ³Electron Microscopy Laboratory, Peking University, Beijing 100871, China

8 ⁴Key Laboratory for Meteorological Disaster Monitoring and Early Warning and Risk Management of Characteristic
9 Agriculture in Arid Regions, China Meteorological Administration, Yinchuan 750002, China

10 *Corresponding author: Qinghong Zhang (qzhang@pku.edu.cn); Kai Bi (bikai_picard@vip.sina.com)

11

12 **Abstract.** Insoluble particles influence weather and climate by heterogeneous freezing process. Current weather and climate
13 models face considerable uncertainties in freezing processes simulation due to limited information regarding species and
14 number concentration of heterogeneous ice-nucleating particles, particularly insoluble particles. Here, for the first time, size
15 distribution and species of insoluble particles are analyzed in 30 shells of 12 hailstones collected from China, using scanning
16 electron microscopy and energy dispersive X-ray spectrometry. A total of 289,461 insoluble particles were detected and
17 identified into 3 species: organics, dust, and bioprotein, utilizing machine learning methods. The size distribution of insoluble
18 particles of each species varies greatly among the different hailstones but little in their shells. Further, classic size distribution
19 of organics and dust followed logarithmic normal distributions, which could potentially be adapted in future weather and
20 climate models, despite the existence of uncertainties. Our finding suggests the aerosol species and number concentration
21 variance in different storms should be considered in model simulation of the ice freezing process.

22 **1 Introduction**

23 Insoluble particles, acting as main heterogeneous ice-nucleating particles in the atmosphere(Lamb and Verlinde, 2011),
24 influence precipitation formation and radiative forcing (Hoose and Möhler, 2012; DeMott et al., 2015), and further impact
25 weather and climate (Vergara-Temprado et al., 2018). Temperature and vapor supersaturation are used to calculate the number
26 concentration of ice crystal particles in microphysics parameterization rather than considering the physical properties of ice-
27 nucleating particles in weather and climate models (DeMott et al., 2010). Few models used the freezing parameterization,
28 which establishes a direct connection between the number concentration of ice-nucleating particles and the number
29 concentration of ice crystals. The absence of description regarding the number concentration of ice-nucleating particles in
30 models can result in an incorrect estimation of ice crystals and lead to significant bias in radiative simulations (Vergara-
31 Temprado et al., 2018).

32 An improved description of the number concentrations of ice-nucleating particles is needed (DeMott et al., 2010), while
33 obstructed by a lack of complete microphysical observation in clouds about ice-nucleating particles. There are two ways to
34 sample ice-nucleating particles: The first involves an airborne instrument, named continuous flow thermal gradient diffusion
35 chamber (Rogers et al., 2001; Prenni et al., 2009; DeMott et al., 2010). The second is done in the laboratory, where scientists
36 conduct freezing experiments (Hoose and Möhler, 2012). In most cases, it is necessary for an aircraft to collect air parcels for
37 measurement of the physical properties of ice-nucleating particles in the air. However, former field projects sampled air parcels
38 in anvils of convective clouds, cirrus and winter mixed-phase stratiform clouds. No flight report or article has reported that
39 they sampled air parcels through cores in deep convection. This phenomenon is consistent with consideration for flight security.
40 Thus, current observation is insufficient for describing the whole convective cloud, especially the deep convection in severe
41 storms. Absence about microphysical observations of ice-nucleating particles within severe storms leads to uncertainty in

42 understanding cold cloud process.

43 Hailstones, as a product of deep convective clouds, serves as a carrier of information within these clouds. Recently,
44 analysis revealed large diversity in number concentration of soluble ions among hailstones from different hailstorms (Li et al.,
45 2018). Further, the detection of soluble ions along with isotopic analysis of a huge hailstone revealed an up-and-down hailstone
46 growth trajectory, which demonstrated that the different shells were formed at different heights (Li et al., 2020). These studies
47 have proved that aerosol information in convective cloud may be recorded in soluble particles within hailstones (Li et al., 2018,
48 2020). Similarly, insoluble particles in hailstones can also record aerosol information in severe storms.

49 Former studies showed that species and number concentration of insoluble particles in hailstones (Vali, 1968; Rosinski,
50 1966; Michaud et al., 2014) would influence heterogeneous nucleation process (Hoose and Möhler, 2012) and further hailstone
51 formation (Knight, 1981). Information on the species of insoluble particles can determine the freezing temperature when these
52 particles participate in the initiation of ice crystal formation and subsequently impact hailstone embryo growth. Biological
53 particles in hailstones, such as pollen and bacteria, are more efficient ice-nucleating particles than dust within the ice nucleation
54 region of storm clouds (Michaud et al., 2014). They can raise the freezing threshold temperature above $-15\text{ }^{\circ}\text{C}$, while dust
55 particles are activated to form ice crystals at temperatures below $-15\text{ }^{\circ}\text{C}$ (Michaud et al., 2014). In addition to species, number
56 concentration of insoluble particles can also influence the hailstone formation. When more dust particles were considered, a
57 model simulation resulted in larger number concentration of ice crystals, smaller graupels (one type of hailstone embryos) size,
58 and suppression of the hailstone growth (Chen et al., 2019). Nonetheless, previous studies involving analysis of insoluble
59 particles in hailstones mainly focused on substances analysis or total number concentration statistics. A size distribution of
60 insoluble particles in hailstones with species information, which is beneficial for completing microphysical observation in
61 severe storms, has not been given so far.

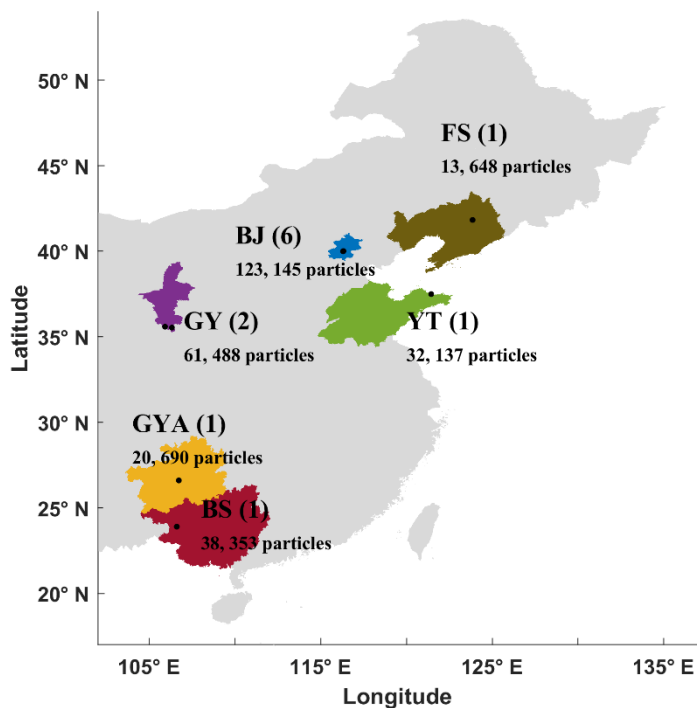
62 This study analyzed insoluble particles in hailstones collected from 8 hailstorms that occurred in China between 2016
63 and 2021. The identification of insoluble particles in hailstones was conducted using Scanning Electron Microscopy (SEM)
64 and Energy Dispersive X-ray spectrometry (EDX). The insoluble particles were identified into three species using Self-
65 Organized Maps (SOMs) and the random forest method. The variation in size distribution of insoluble particles in embryos
66 and different shells was explored. Based on the size distributions, logarithmic normal distributions were fitted to describe the
67 concentration of organics and dust in deep convection.

68 **2 Methods**

69 **2.1 Sample information and experimental design**

70 Hailstones were collected from eight hailstorms that occurred in six provinces of China during warm seasons from 2016
71 to 2021 (Table 1, Fig. 1). Volunteers stored the hailstones in clean containers, including plastic bags, glass containers, and

72 tinfoil, either during or immediately after the hail events. All hailstone samples were transported to a laboratory at Peking
73 University in Beijing and kept at temperatures ranging from -18 °C to -4 °C. The hailstones were then transferred into vacuum-
74 sealed plastic pockets and preserved in a freezer, maintaining an internal temperature ranging from -29°C to -23°C, until they
75 underwent further processing and analysis.



76
77 **Fig. 1: Geographical distribution of collected hailstones. The collecting locations of hailstones are indicated by black dots. Provinces**
78 **of China from which the hailstones were collected are represented by six different colors. The number of hailstones we analyzed was**
79 **indicated in parentheses. Abbreviations (corresponding to Table 1): BJ - BeiJing; BS - BaiSe; FS - FuShun; GY - GuYuan; GYA -**
80 **GuiYAng; YT - YanTai.**

Table 1: Information about collected hailstones.

Date & Beijing Local Time ^a	Latitude & Longitude ^b	Total column water vapor ^c (kg / m ²)	Freezing level height – orography altitude ^d (m)	Location & Sample abbreviation ^e	Samples ^f	Diameter ^g (mm)	Particle number ^h
19 June 2018, 18:30	41.82° N, 123.85° E	26.35 ^[18]	3241.66 ^[18]	FuShun (FS)	1	13.80	13,648
10 June 2016, 15:00	40.00° N, 116.32° E	36.86 ^[14]	3780.52 ^[14]	BeiJing (BJ1)	1	—	35,291
30 June 2021, 20:18	39.95° N, 116.30° E	31.84 ^[20]	3852.76 ^[20]	BeiJing (BJ2)	5	25.38	14,865
				BeiJing (BJ3)		24.11	20,233
				BeiJing (BJ4)		16.30	20,350
				BeiJing (BJ5)		14.86	14,350
				BeiJing (BJ6)		22.80	18,056
01 Oct 2021, 14:02	37.49° N, 121.44° E	32.81 ^[13]	3642.42 ^[13]	YanTai (YT)	1	45.00	32,137
25 Aug 2020, 18:00	35.53° N, 106.32° E	17.83 ^[17]	422.58 ^[17]	GuYuan (GY1)	1	15.00	29,341
26 Aug 2020, 16:00	35.58° N, 105.93° E	17.01 ^[15]	835.04 ^[15]	GuYuan (GY2)	1	18.50	32,107
14 Apr 2016, 20:00	26.60° N, 106.72° E	31.62 ^[19]	2147.58 ^[19]	GuiYAng (GYA)	1	26.20	20,690
09 May 2016, 18:51	23.90° N, 106.60° E	47.45 ^[18]	4572.70 ^[18]	BaiSe (BS)	1	—	38,353

^a Date and Beijing local time of hailstorms occurrences. Hailstones were collected within 30 min during hail.

^b Latitude and longitude where the hailstone were collected.

^c Total column water vapor values (Beijing local time of ERA5 reanalysis data in square brackets (Hersbach et al., 2018)).

^d Depth between freezing level and orography (Beijing local time of ERA5 reanalysis data in square brackets(Hersbach et al., 2018)).

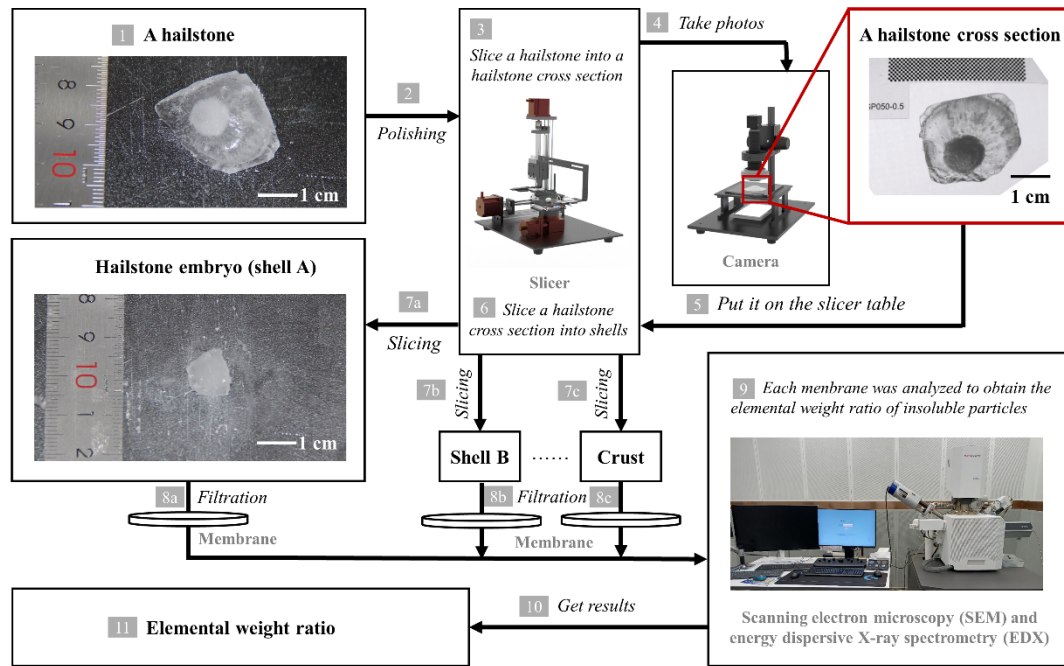
^e Location and sample abbreviations.

^f Numbers of hailstones used in the experiments.

^g Diameter of hailstone (— means no record).

^h Insoluble particle number in hailstones.

83 Insoluble particles were extracted in the experiments (Fig. 2). The surface of each hailstone was polished to remove any
 84 attached grass or soil. Subsequently, the hailstones were sliced into cross-sections along the major axis, corresponding to the
 85 size of the hailstone embryo. The cross-section were further sliced into shells using heated Fe-Cr alloy wire at an air
 86 temperature below -8°C . The shells within a hailstone were distinguished based on their natural transparency or opacity.
 87 However, hailstones with a major axis < 7 mm could not be sliced due to the mass loss resulting from heating using our
 88 experimental apparatus.



89
 90 **Fig. 2: Schematic diagram illustrating the experimental framework. [1-2] The surface of each hailstone was polished to remove any**
 91 **attached grass or soil. [3] Subsequently, the hailstones were sliced into cross-sections along the major axis, corresponding to the size**
 92 **of the hailstone embryo. [4-7] After photographing the hailstone cross-sections, they were further subdivided into shells using heated**
 93 **Fe-Cr alloy wire at an air temperature below -8°C . The shells were distinguished based on their natural transparency or opacity. [8]**
 94 **The solution of melting shell samples was then passed through a filter membrane to isolate the insoluble particles. [9] Each shell**
 95 **sample underwent analysis using scanning electron microscopy and energy-dispersive X-ray spectrometry to determine the**
 96 **elemental weight ratios of the insoluble particles within approximately 4 hours. [11] Finally, the elemental weight ratio information**
 97 **of hailstones was obtained.**

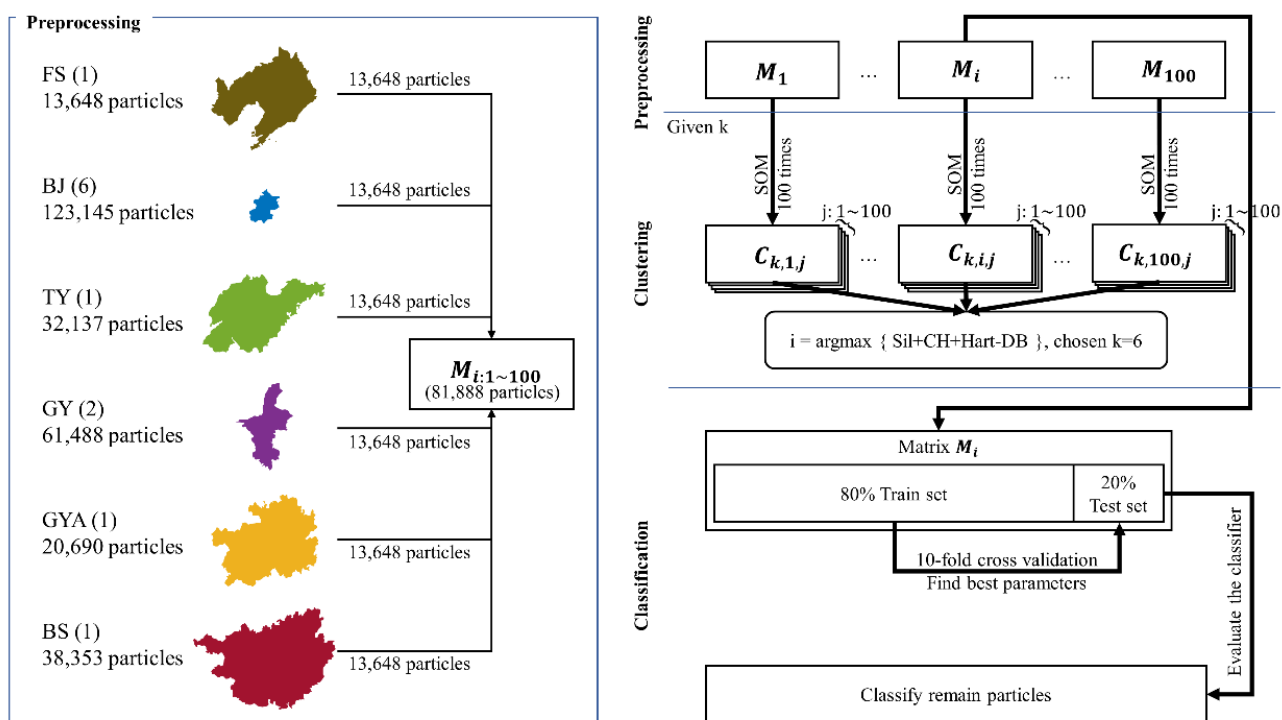
98
 99 The shells were sequentially labeled with capital letters in alphabetical order, starting from the embryo (designated as
 100 shell A) and progressing toward the crust. After the ice shells melting into a solution, the solution was filtered through a
 101 membrane (VSWP01300, Merck KGaA, Germany) with a pore size of 30 nm. The 1 mL (a total of 5 mL) of distilled water
 102 underwent five passes through the filter membrane to ensure maximum retention of insoluble particles on the membrane.

103 Subsequently, the filter membrane was dried under an air temperature of approximately 40°C to satisfy the dry-environment
 104 requirements of SEM.

105 The number of insoluble particles in each shell was determined using scanning electron microscopy (SEM), with a focus
 106 on particles larger than 0.16 μm. The length along the major axis of the particles was measured using Aztec software (Aztec
 107 software, Oxford Instruments plc, UK) on SEM images. The software was able to randomly capture electron microscopy
 108 photos of the membrane (Aztec User Manual). No particle will be counted repeatedly. Energy-dispersive X-ray spectrometry
 109 (EDX) was utilized to determine the elemental weight ratios of the particles. Only elements with an atomic number greater
 110 than 4 could be detected due to the X-ray input window being made of beryllium. Each shell sample was analyzed within
 111 approximately 4 hours by SEM and EDX. The scanning mode of SEM was set in a random order to reduce errors caused by
 112 bias in the detection area.

113 2.2 Clustering and classification

114 The number of insoluble particles was measured using Aztec on SEM images, but the species could not be determined
 115 directly and were identified by machine learning method. The criteria of species classification were established by the SOMs
 116 method to determine the species of unclassified particles. These labeled particles were then regarded as training set in random
 117 forest classifier. Details are presented in Fig. 3.



118
 119 **Fig. 3: Schematic diagram illustrating the methodological framework used for particle identification in this study. A total of 100**
 120 **matrices M_i , with i ranging from 1 to 100, were utilized in self-organized maps clustering analyses, each containing 81,888**
 121 **unidentified particles with 19 elemental features (N, Na, Mg, Al, Si, P, S, Cl, K, Ca, Ti, Cr, Mn, Fe, Ni, Cu, Br, Ba, and Pb). The**
 122 **centroid matrix $C_{k,i,j}$ represents the clustering results obtained through the self-organized maps method with a given cluster**

123 number k . The self-organized maps operation with the same k was repeated 100 times to ensure result robustness, where j
124 denotes the number of repetitions ranging from 1 to 100. Four indices, Silhouette index (Sil), Calinski–Harabasz index (CH),
125 modified Hartigan index (Hart), and Davies–Bouldin index (DB), were employed to determine the optimal parameters k , i , and j .
126 The matrix \mathbf{M}_i containing identified 81,888 particles was randomly divided into a training set (80 %) and a test set (20 %) for
127 random forest classification. The 10-fold cross-validation was utilized to determine the best tree. Abbreviations (corresponding to
128 Table 1): BJ - BeiJing; BS - BaiSe; FS - FuShun; GY - GuYuan; GYA - GuiYAng; YT - YanTai.

129
130 With reference to the studies of Ault et al. (2012) and Kirpes et al. (2018) and considering the results of elemental weight
131 ratios determined by EDX analysis, 19 elements (N, Na, Mg, Al, Si, P, S, Cl, K, Ca, Ti, Cr, Mn, Fe, Ni, Cu, Br, Ba, and Pb)
132 were selected to confirm the species of particles. C and O were not taken in account when clustering or classifying particles as
133 the membrane filters were made from cellulose acetate and cellulose nitrate, which contain C, H, N, and O. We could not detect
134 H because the ray-input window was made of beryllium. All particles showed high contents of C and O but different contents
135 of N, so N was retained as a feature of classification.

136 Species of aerosol particles vary with sampling location (Tao et al., 2017). Therefore, when establishing the matrices
137 of elemental weight ratios for clustering, equal amounts of data were randomly extracted from the sample data from each
138 province to ensure the inclusion of a consistent proportion of samples from each region in the training process. A hailstone FS
139 collected from Fushun City, Liaoning Province was shown to contain 13,648 insoluble particles, which was the smallest among
140 all samples from six provinces (Fig. 1). With random sampling of 13,648 particles from each province, the matrix used in
141 clustering analyses included 81,888 particles. This operation was repeated 100 times to obtain 100 matrices \mathbf{M}_i with i
142 ranging from 1 to 100.

143 Each matrix \mathbf{M}_i was clustered using the SOMs method. SOMs belong to the category of competitive learning algorithms
144 and are a type of artificial neural network (Kohonen, 1990). A basic SOMs network consists of an input layer, weight vectors,
145 and an output layer. Each neuron in the output layer possesses a set of weight vectors, which represent the topological structure
146 of the neurons in the output layer, associated with the inputs. SOMs are commonly used as dimensionality reduction algorithms,
147 enabling the representation of high-dimensional data in a lower-dimensional structure while preserving the original topology.
148 When SOMs are trained on unlabeled data for clustering purpose, it proves highly beneficial in clustering unlabeled and high-
149 dimensional inputs into visualized two-dimensional outputs.

150 We utilized the SOMs code from MATLAB's deep learning toolbox. The input of SOMs is \mathbf{M}_i . At begin, the neural
151 network in the output layer was initialized as 1-D dimension with k neurons. The number of neurons in the output layer
152 matches k ranging from 2 to 10. The operation of SOMs with the same initialized k neurons and input matrix \mathbf{M}_i was
153 repeated 100 times to ensure result robustness. The clustering result was stored in matrix $\mathbf{C}_{k,i,j}$, which corresponded to the

154 given k centroids in \mathbf{M}_i with j^{th} SOMs operation. Each $\mathbf{C}_{k,i,j}$ matrix consists of k rows and 19 columns (corresponding
155 to the number of elemental features). Four indices, namely, the Silhouette index (Rousseeuw, 1987), the Calinski–Harabasz
156 index (Calinski and Harabasz, 1974), the modified Hartigan index (Sibson and Hartigan, 1976), and the Davies–Bouldin index
157 (Davies and Bouldin, 1979), were selected as evaluation indicators to determine the parameters k , i and j . The Silhouette
158 index, Davies–Bouldin index, and Calinski–Harabasz index assess the similarity between a particle and others within the same
159 cluster, as well as the dissimilarity across different clusters for a given k . Hartigan index evaluates whether it is worthy to
160 increase the k . Notably, Hartigan index has undergone modifications that preserve its statistical meaning while conserving
161 computational resources.

162 Hartigan index (Sibson and Hartigan, 1976) is defined as:

$$163 \quad H(k) = (N - k - 1) \left[\frac{err(k)}{err(k+1)} - 1 \right], k = 2 \sim 10 \quad (1)$$

$$164 \quad err(k) = \sum_{g=1}^k \sum_{x_g \in C_g} (x_g - C_g)^2 \quad (2)$$

165

166 k : the number of clusters.

167 C : the centroid of all data

168 N : the number of observations in data

169 C_g : the centroid of cluster g

170 x_g : the observation of cluster g

171 x_n : the observation of data

172 The calculation of $H(k)$ requires clustering for values of k ranging from 2 to 11 in order to obtain $H(2)$, $H(3)$, ...,
173 $H(10)$. Clustering particles into 11 clusters would require performing an additional 10,000 iterations of the SOMs, with 100
174 iterations of extracting \mathbf{M}_i and 100 iterations of SOMs for each \mathbf{M}_i . Additionally, we observed that the SOMs did not perform
175 well in the Silhouette index (Sil), the Calinski–Harabasz index (CH), and the Davies–Bouldin index (DB) when $k = 2$. As a
176 result, we introduced modifications to the Hartigan index.

$$177 \quad Hart(k) = [N - (k - 1) - 1] \left[\frac{err(k-1)}{err(k)} - 1 \right], k = 2 \sim 10 \quad (3)$$

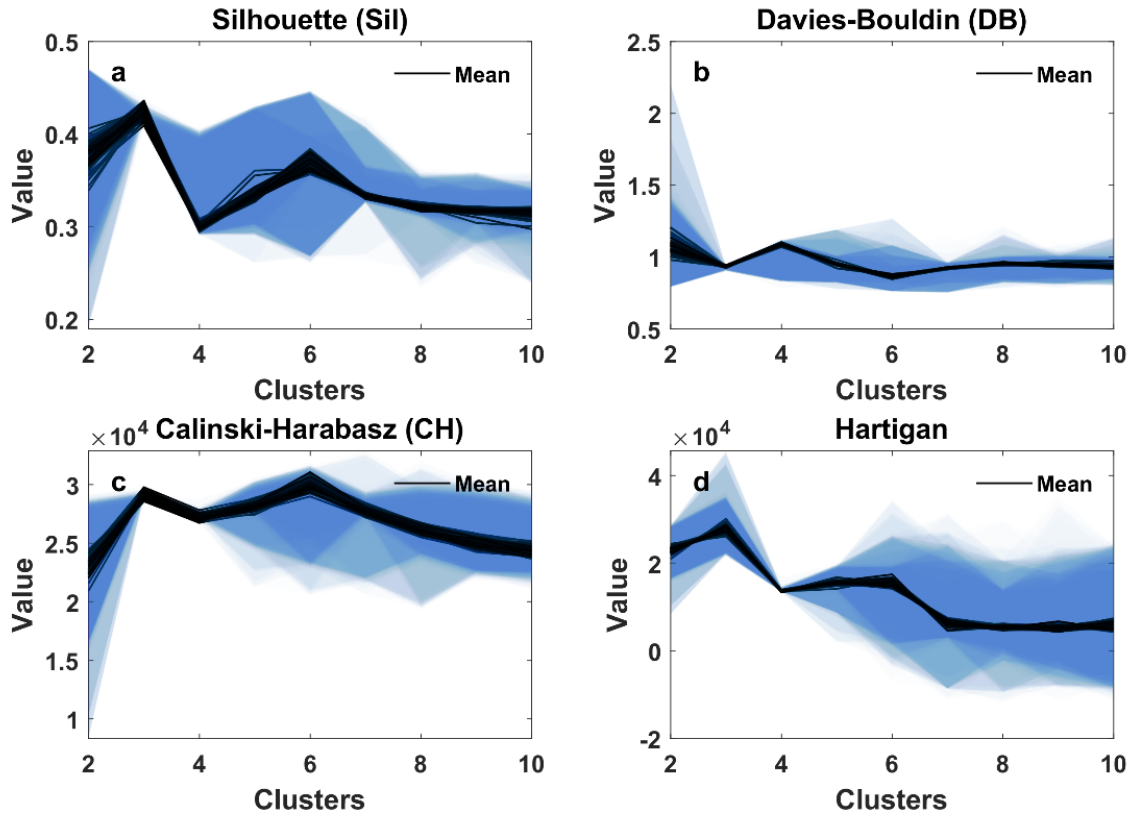
$$178 \quad err(k) = \sum_{g=1}^k \sum_{x \in C_g} (x_g - C_g)^2, k \geq 2 \quad (4)$$

179

180 When $k = 1$, it indicates that all particles are belong to one cluster.

$$181 \quad err(1) = \sum_{n=1}^N (x_n - C)^2 \quad (5)$$

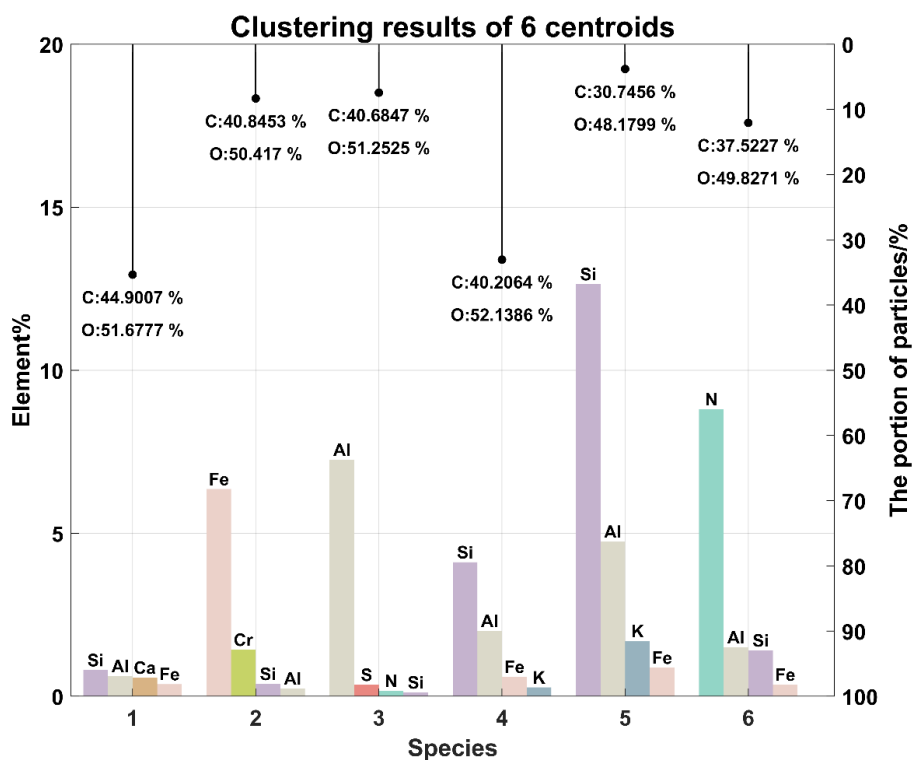
182 In clustering with a specific value of k , our objective is to have particles tightly grouped together in feature space while
 183 ensuring that the centroids exhibit a significant dispersion compared to $k - 1$. A higher value of $Hart(k)$ for a given k
 184 indicates improved clustering performance. The best k , i and j was chosen by combining the evaluation of the four indices
 185 (Fig. 4). We applied max normalization to rescale the four indices, $Sil(k)$, $CH(k)$, $DB(k)$, and $Hart(k)$. Subsequently, the
 186 best combination of k , i and j was determined, resulting in $\{Sil(k, i, j) + CH(k, i, j) + Hart(k, i, j) - DB(k, i, j)\}$
 187 reaching its maximum.
 188



189
 190 **Fig. 4: Evaluation of self-organized maps clustering results.** The clustering results of self-organized maps were evaluated using (a)
 191 **Silhouette index, (b) Davies–Bouldin index, (c) Calinski–Harabasz index, and (d) Hartigan index.** The self-organized maps operation
 192 was repeated 100 times to ensure result robustness. The solid lines and shading represent the average and spread of 100 repetitions,
 193 respectively.
 194

195 The centroid matrix $\mathbf{C}_{k,i,j}$ with best k , i and j was treated as a training set for random forest classification. The chosen
 196 centroid matrix $\mathbf{C}_{k,i,j}$ with the top four elements is shown in Fig. 5 with $k = 6$. The first species with low elemental weight
 197 ratio except C and O contents was considered to be organics. The second species with high Fe content and low Cr content was
 198 introduced by the material of the slicer used in the experiment. The third species had a high Al content representing oxides or
 199 carbonates of aluminum. The fourth and fifth species were mineral silicates. So that, the third, fourth, and fifth species were

200 referred to as “dust”. The last species with high N content was protein-containing biological aerosol.



201
 202 **Fig. 5: Centroids of clustering with six clusters from self-organized maps results and each species portion. Colored bars show the**
 203 **top four elements of each species. The stem bars show the portion of each species. The average contents of C and O of each species**
 204 **are marked at the end of the stem bars.**

205
 206 The random forest method was applied in classifying insoluble particles, which involves randomly growing 100
 207 classification trees. The training set consisted of 80 % of M_i and 10-fold stratified cross-validation was applied during the
 208 training process to find the best tree among the 100 random trees. The remaining 20 % particles of M_i was used as the test set
 209 to evaluate the best tree. The confusion matrix of classification results are shown in Fig. 6. All remaining insoluble particles
 210 were classified by this tree. Finally, we identified three species: organics, dust, and bioprotein aerosols.

		Insoluble Particle Classification						Recall	
True type	1	937	7					99.3%	0.7%
	2	5	6076	1	28	5		99.4%	0.6%
	3		2	786			2	99.5%	0.5%
	4		41		4577	19		98.7%	1.3%
	5	1	11		7	2967		99.4%	0.6%
	6			2			904	99.8%	0.2%
		99.92%	99.39%	99.96%	99.42%	99.74%	99.98%		
Precision		99.4%	99.0%	99.6%	99.2%	99.2%	99.8%		
		0.6%	1.0%	0.4%	0.8%	0.8%	0.2%		
		1	2	3	4	5	6		
		Predicted type							

Fig. 6: Confusion matrix of the best random forest classifier tree. The numbers on the diagonal are accurately predicted insoluble particles. Numbers in bold indicate the accuracy of prediction of each type.

2.3 Conversion of insoluble particle number concentration

Particle number was converted to a number concentration per cubic centimeter volume water (hereinafter referred to as number concentration) using the following formula:

$$n_{liquid} \cdot V_{liquid} = N_{liquid} = N_{diluted} = n_{diluted} \cdot V_{diluted} \quad (6)$$

The number of insoluble particles in the melted shell solution (N_{liquid}) can be calculated by multiplying their number concentration (n_{liquid}) with the volume of the shell solution (V_{liquid}). Part of the solution was not used up in the experiments and was kept as a backup. Therefore, the shell solution was diluted in some experiments and part of the solution was consumed in the experiments. As in the melting solution, the number of insoluble particles in the diluted solution ($N_{diluted}$) can be calculated by multiplying their number concentration ($n_{diluted}$) with the volume of the diluted solution ($V_{diluted}$). The total particle number in the melted shell (N_{liquid}) remains unchanged during the dilution process ($N_{diluted}$).

$$n_{diluted} = n_{used} = \frac{N_{used}}{V_{used}} \quad (7)$$

The number concentration of the diluted solution ($n_{diluted}$) is equal to that of the consuming part (n_{used}). Assuming the rinsing operation ensures all insoluble particles in the shell were on the membrane, the number of insoluble particles in the consumed solution (N_{used}) is equal to the number of insoluble particles counted on the membrane (N_{filter}).

We use SEM to capture electron microscopy images of the membrane. Assuming a uniform distribution of insoluble

230 particles on the filter membrane, a software randomly capture electron microscopy photos of the membrane and count the
 231 visible insoluble particles in those images. The relationship between total number of visible insoluble particles counted in the
 232 images (N_{count}) and N_{filter} is:

$$233 \quad \frac{S_{images}}{S_{filter}} = \frac{N_{count}}{N_{filter}} \quad (8)$$

234 That is, N_{filter} is determined by multiplying N_{count} by the ratio of the areas between the entire filter membrane (S_{filter})
 235 and the electron microscopy images (S_{images}). These three formulas Eq. (6-8) were reduced to Eq. (9):

$$236 \quad n_{liquid} = \frac{1}{V_{liquid}} \cdot \frac{S_{filter}}{S_{images}} \cdot \frac{V_{diluted}}{V_{used}} \cdot N_{count} \quad (9)$$

237 Here, S_{filter} , S_{images} , N_{count} , $V_{diluted}$, and V_{used} can be measured. The liquid volume (V_{liquid}) was determined as the
 238 average of readings obtained by two experimenters from the test tube. Take the logarithm on both sides:

$$239 \quad \ln n_{liquid} = -\ln V_{liquid} + \ln S_{filter} - \ln S_{images} + \ln V_{diluted} - \ln V_{used} + \ln N_{count} \quad (10)$$

240 Based on Eq. (10), a tiny change in n_{liquid} can be represented as dn_{liquid} :

$$241 \quad dn_{liquid} = n_{liquid} \cdot \left(-\frac{dV_{liquid}}{V_{liquid}} + \frac{dV_{diluted}}{V_{diluted}} - \frac{dV_{used}}{V_{used}} + \frac{dN_{count}}{N_{count}} \right) \quad (11)$$

242 As,

$$243 \quad dS_{filter} = dS_{images} = 0 \quad (12)$$

244 The uncertainty (Δ) of n_{liquid} comes from the measurement error of the experimental instruments, following below
 245 (Taylor, 1997):

$$246 \quad \Delta = n_{liquid} \cdot \sqrt{\left(\frac{dV_{liquid}}{V_{liquid}}\right)^2 + \left(\frac{dV_{diluted}}{V_{diluted}}\right)^2 + \left(\frac{dV_{used}}{V_{used}}\right)^2 + \left(\frac{dN_{count}}{N_{count}}\right)^2} \quad (13)$$

247 Here, the accuracy of the test tube is 0.1 mL. The term dV represents the greatest reading error caused by human and
 248 was set to 0.05 mL. The quantity $\frac{dN_{count}}{N_{count}}$ corresponds to the uncertainty associated with size of insoluble particles and the
 249 scan settings.

$$250 \quad \frac{dN_{count}}{N_{count}} = \frac{dPs}{Ps} = \frac{3}{6,340,608} \quad (14)$$

251 The term dPs represents the minimum number of pixels that can be detected in an image. Ps denotes the total number
 252 of pixels in the micrograph.

253 2.4 Curves fitting

254 We aggregated insoluble particles into 0.2- μm intervals (0.2 μm bin interval in Fig. 7 and Fig. 10, and 2 μm bin interval
 255 in Fig. 8 and Fig. 9) to fit the logarithmic normal distribution:

$$256 \quad n(\ln D) = \frac{N}{\sqrt{2\pi} \ln \sigma_g} \cdot \exp \left[-\frac{(\ln D - \ln D_g)^2}{2 \ln^2 \sigma_g} \right] \quad (15)$$

257 N denotes the total number concentration of particles. Both $n(\ln D)$ and $n(D)$ represent the size distributions of
258 particles, where D is the diameter of insoluble particles. $n(\ln D)$ and $n(D)$ can be converted to each other by D .

$$259 \quad n(D) = \frac{1}{D} \cdot n(\ln D) \quad (16)$$

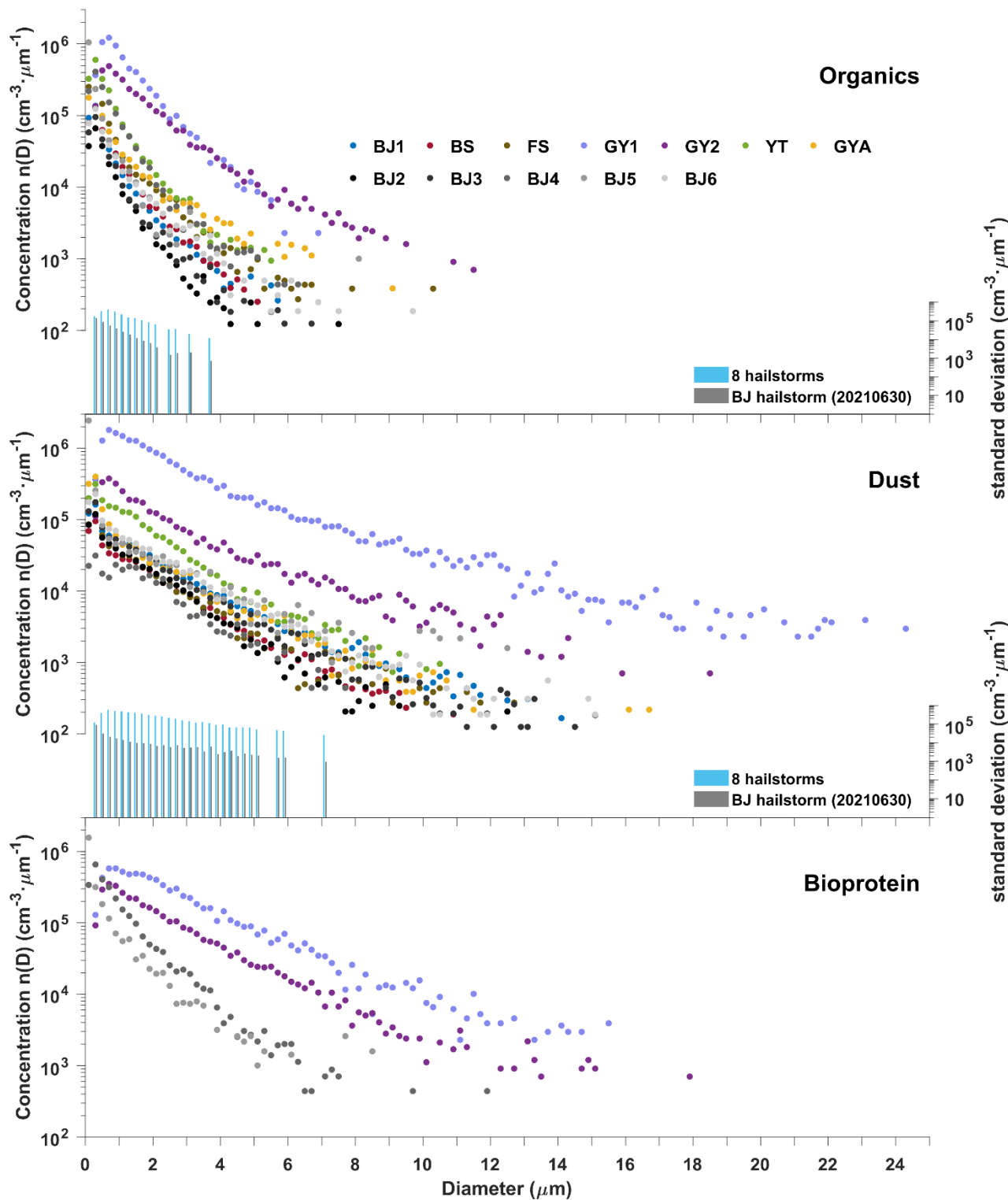
260
261 When the N_{count} in an interval equals 1, the number concentration will exhibit a flat tail due to the conversion to obtain
262 n_{liquid} . The fitting data were selected with intervals equals to 0.2 μm . The least squares method was applied to determine the
263 fitting parameters and R^2 was used to estimate the goodness of fit. The two centroids of fitting parameters of organics and dust
264 were determined by K-means method.

265 **3 Results**

266 A total of 289,461 insoluble particles were detected from 30 shells of 12 hailstones using SEM. The identification of
267 insoluble particles employed SOMs for clustering and random forest for classification. Four indices were utilized to determine
268 the appropriate parameters in clustering. The clustering results ($C_{k,i,j}$) were divided into a training and a testing set for
269 classification. The confusion matrix of the best classifier showed an accuracy, precision, and recall of 99.7 %, 99.4 %, and
270 99.5 %, respectively. All particles were classified as organics, dust, and bioprotein aerosols (i.e., the fraction of biological
271 aerosols with protein content).

272 **3.1 Sample similarity**

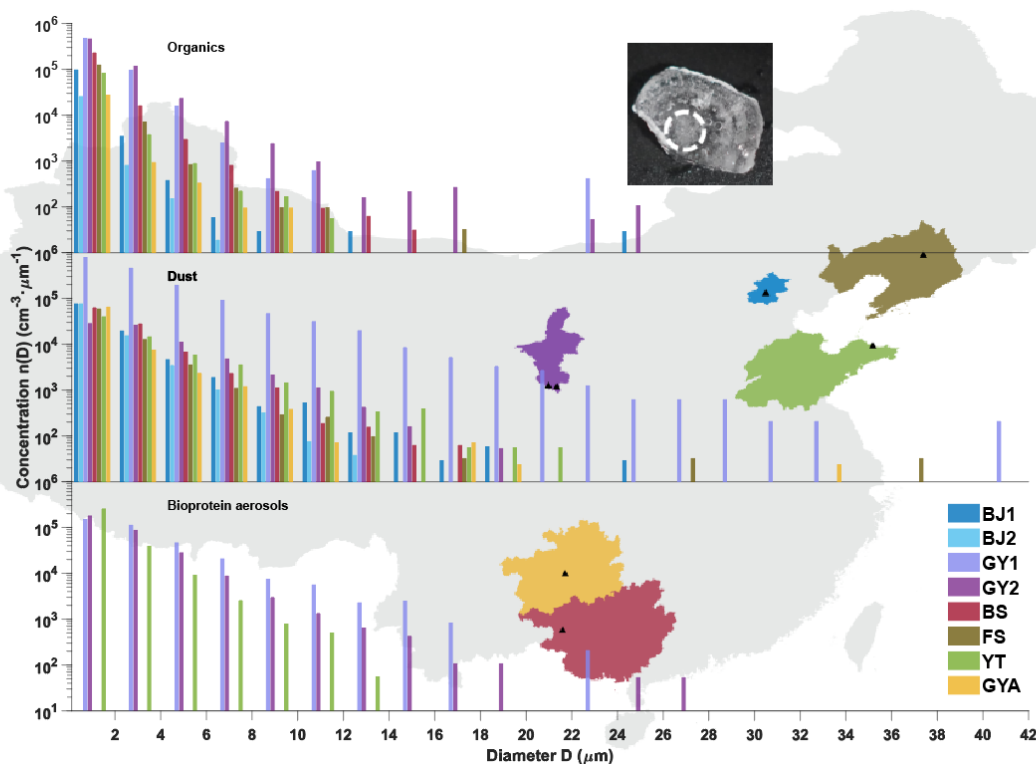
273 Five of the 12 hailstones (BJ2–BJ6) were from the same hailstorm that occurred in Beijing on June 30, 2021. The insoluble
274 particles present in BJ2–BJ6 showed similarity in the size distribution of organics, dust, and bioprotein aerosols, while those
275 from 8 hailstones (BJ1, BJ2, BS, FS, GY1, GY2, YT and GYA) exhibited a wider dispersion (Fig. 7). The results were similar
276 to those of Li et al., who reported that the number concentrations of water-soluble ions varied among hailstorm events but
277 showed similarity in the same storm (Li et al., 2018). These analyses suggested that insoluble particles in the hailstorm may
278 come from local natural or anthropogenic emissions (e.g., soil dust, aerosols from biomass and fossil fuel combustion, products
279 of the conversion of gaseous precursors), which is also suggested by the results on water-soluble ions (Beal et al., 2022). The
280 updraft within the hailstorm is likely to bring insoluble particles from local surfaces or boundary layers into deep convective
281 clouds, as hailstorms are among the most severe storms with strong updrafts (Battaglia et al., 2022).



282
 283 Fig. 7: Size distribution of organics, dust, and bioprotein aerosols of insoluble particles in 12 hailstones. The colored dots represent
 284 data from 7 hailstones BJ1, BS, FS, GY1, GY2, YT and GYA which were from different hailstorms. The black and gray dots
 285 correspond to data from hailstones (BJ2 to BJ6) that were from the same hailstorm occurring in Beijing on June 30, 2021. The blue
 286 and gray bars indicate the standard deviation of number concentration of insoluble particles from 8 hailstones (BJ1, BJ2, BS,
 287 FS, GY1, GY2, YT and GYA) from 8 cases and 5 hailstones (BJ2 to BJ6) from one case, respectively. Abbreviations (corresponding
 288 to Table 1): BJ - BeiJing; BS - BaiSe; FS - FuShun; GY - GuYuan; GYA - GuiYANG; YT - YanTai.

289 **3.2 Size distribution in embryos**

290 All hailstone embryos analyzed in this study are graupel particles, which grows from the initial ice particles through
 291 accretion of supercooled droplets (Knight, 1981). These initial ice particles are formed through nucleation of insoluble particles
 292 where heterogeneous nucleation take place (Lamb and Verlinde, 2011). In other words, insoluble particles in graupels influence
 293 the formation of ice crystals and subsequently affect the formation of hailstone embryos.



294
 295 **Fig. 8: Size distribution of insoluble particles in hailstone embryos. Different colors represent the provinces in China from which**
 296 **the hailstones were collected. Black triangles indicate the locations of hailstone sample collection. The white dashed circle highlights**
 297 **part of the hailstone embryo. Abbreviations (corresponding to Table 1): BJ - BeiJing; BS - BaiSe; FS - FuShun; GY - GuYuan; GYA**
 298 **- GuiYAng; YT - YanTai.**

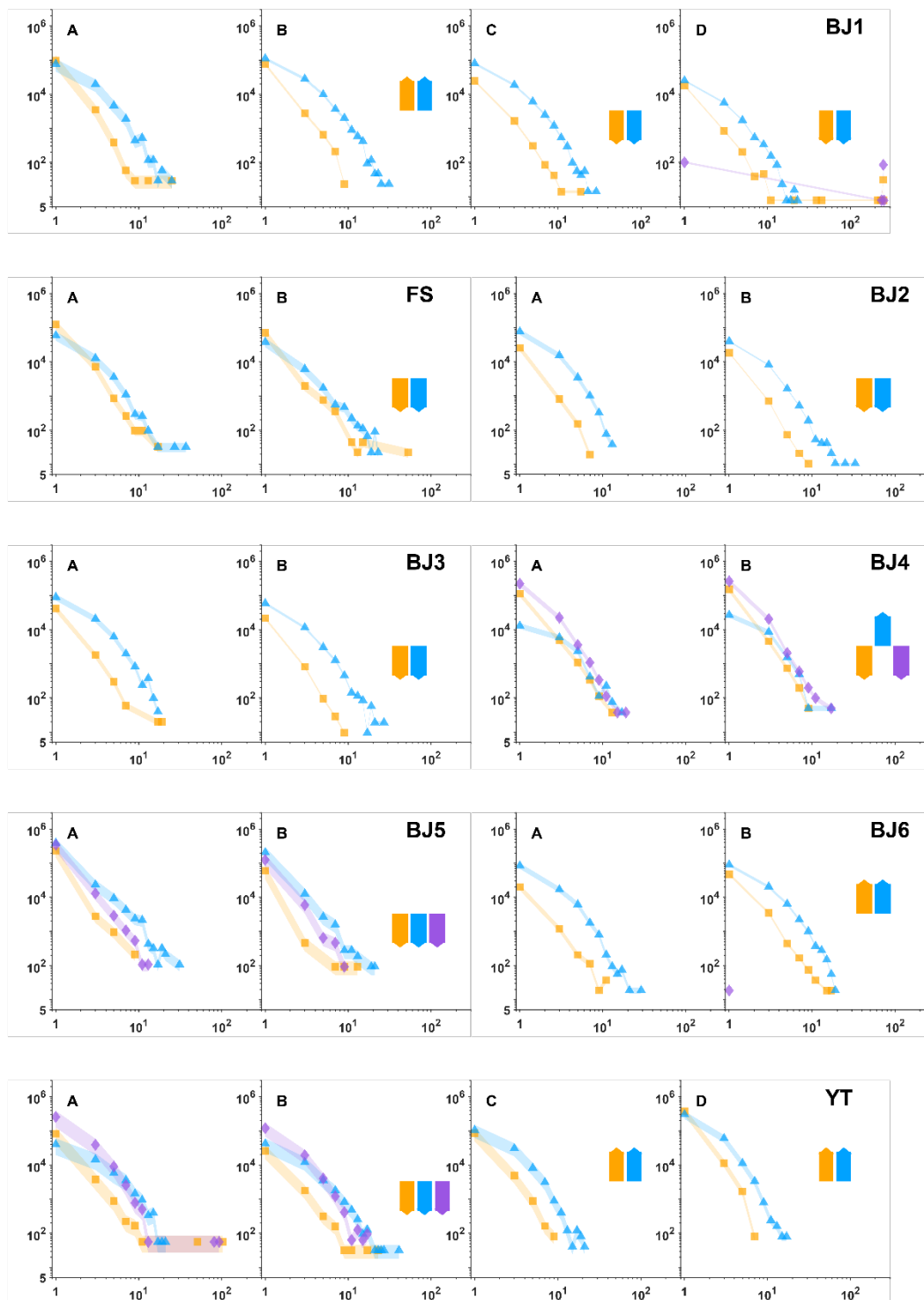
299
 300 The variations in number concentrations of dust and bioprotein insoluble particles indicate that particle number
 301 concentrations decrease exponentially with particle diameter, with markble variation observed among hailstorms (Fig. 8). BJ2
 302 was selected to represent five hailstones from the same storm to simplify comparison. The size distribution distinguishes
 303 organics from dust and bioprotein aerosols. The number concentrations of organics from all samples decrease with particle
 304 diameter less than 8 μm , while those of GY1 and GY2 fluctuate starting at diameters of 8 μm and 12 μm , respectively.
 305 Compared to other hailstones, GY1 and GY2 were collected in remote areas, where is fields of rural areas dedicated to growing
 306 crops near the south of the Gobi Desert. Therefore, GY1 and GY2 have a coarse mode of organics with particle diameters
 307 larger than 12 μm , possibly might due to the emission of spring-wheat straw burning and unrestricted diesel engine vehicles.
 308 The transport of coal combustion in surrounding cities may also contribute to the coarse mode organics. Among all cases, there

309 is a significant variance in the size distribution of both organics and dust. The number concentration of organics from a
310 hailstone embryo varied from 1 to 390 times, compared to those at the same particle diameter in hailstone embryos from
311 different cases. The number concentration of dust from a hailstone embryo varied from 1 to 527 times, compared to those at
312 the same particle diameter in hailstone embryos from different cases. The number concentrations of dust from BJ1, BJ2, and
313 GY1 are at least 3 times higher than organics in particles of the same diameter in the range of 2–24 μm .

314 Moreover, dust showed a wider size distribution than organics and bioproteins among all samples. Dust from GY1 had a
315 higher number concentration and larger maximum size (42 μm) compared to other hailstone embryos. Hailstone samples with
316 high insoluble particle content, i.e., GY1 and GY2, showed significantly lower total column water vapor values and smaller
317 depth between freezing level height and orography within one hour before hailstorm occurrence, compared to other hailstones
318 (Table 1). The competition of condensation and relative shorter updraft pathway might be responsible for the high number
319 concentrations of organics, dust, and bioproteins in GY1 and GY2, as compared with other hailstones. Bioprotein aerosols,
320 with high freezing efficiency, may have formed initial ice particles in GY1, GY2, and YT, while dust or organics formed initial
321 ice particle in hailstorms in the other five cases. All hailstone embryos contained organics and dust, but not all hailstone
322 embryos contained a significant amount of bioprotein aerosols. Due to limited comprehension of the transportation and
323 transformation processes of biological materials, it is challenging that to establish a definitive relationship between biological
324 protein particles and biological aerosols (Fröhlich-Nowoisky et al., 2016).

325 **3.3 Size distribution in shells**

326 Size distribution of each species varied little in characteristics between outer shells with the embryos (Fig. 9). In a four-
327 shell hailstone, the number concentrations of insoluble particles exhibited V-shaped distributions (BS and YT) or inverse V-
328 shaped distributions (BJ1) from embryo to crust. Five of nine two-shell hailstones showed higher number concentrations of
329 dust in crusts than embryos, while seven of them showed higher number concentrations of organics in embryos than crusts.
330 Moreover, the quantification of differences in number concentration varied little among shells. The 90.5 % points showed that
331 differences in number concentration of the same kind particles in a shell compared to the previous shell at the same diameter
332 was within twice (294 data points in Fig. 9). This observation is attributed to the fact that the growth of hailstones beyond the
333 embryo stage relies on the accretion of supercooled water rather than ice crystals (Lamb and Verlinde, 2011). Consequently,
334 the hailstone recorded not only insoluble particles during the embryo formation, but also insoluble particle in the hailstone
335 growth zone throughout the hailstorm. As a result, the size distribution of particles within the entire hailstones may represent
336 the distribution of insoluble particles in deep convection regions where the hailstones went through.



337

338

339

340

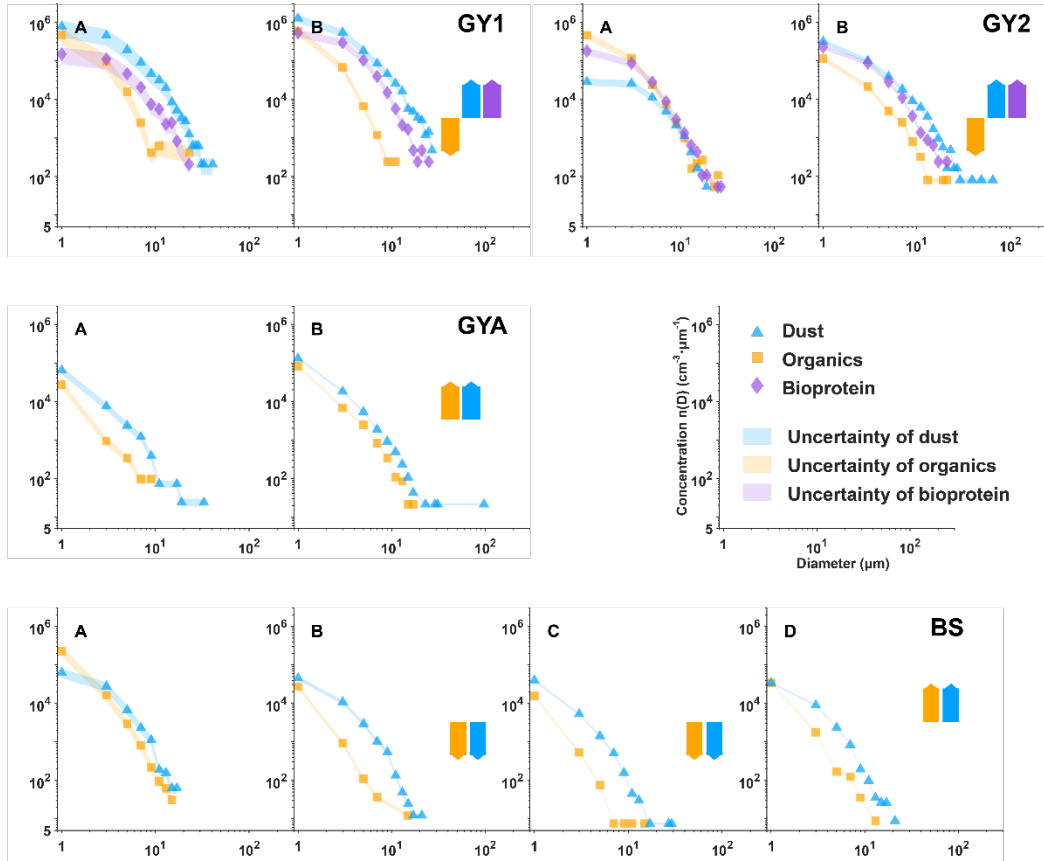
341

342

343

344

Fig. 9a. Size distribution of insoluble particles within the natural shells of 12 hailstones is represented. Blue triangles, orange squares, and purple diamonds are used to indicate dust, organics, and bioprotein aerosols, respectively. The natural shells are denoted alphabetically with capital letters (shell A refers to embryos, and shell B/D refers to the crust of hailstones). The arrow direction illustrates the tendency of particle number concentration in each layer compared to the previous shell. Shading is employed to indicate uncertainty. Detailed calculations are provided in the supplementary information. Abbreviations (corresponding to Table 1): BJ - BeiJing; BS - BaiSe; FS - FuShun; GY - GuYuan; GYA - GuiYAng; YT - YanTai.



345

346 **Fig. 9b is a continuation of Fig. 9a.**

347

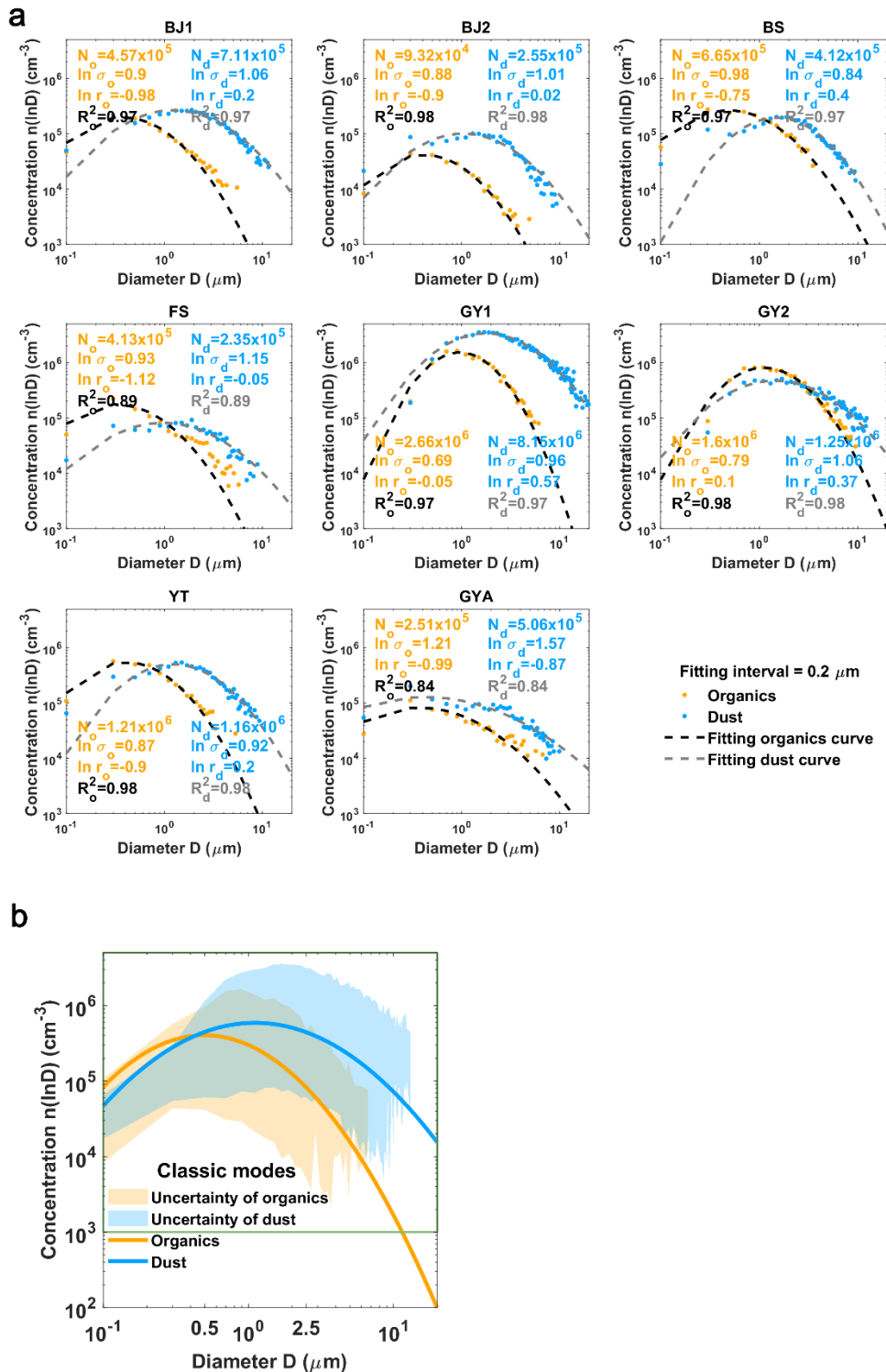
348 **3.4 Logarithmic normal distribution of dust and organics**

349 The size distributions of dust and organics in the whole hailstone can be described by a logarithmic normal distribution
 350 (Fig. 10a) (Lamb and Verlinde, 2011):

$$351 \quad n(\ln D) = \frac{N}{\sqrt{2\pi \ln \sigma_g}} \cdot \exp\left[-\frac{(\ln D - \ln D_g)^2}{2 \ln^2 \sigma_g}\right], (D > 0.2 \mu\text{m}) \quad (17)$$

352 Where $n(\ln D)$ is the number concentration of insoluble particles per cubic centimeter volume water ranging from
 353 $\ln D - \frac{1}{2} \ln \sigma_g$ to $\ln D + \frac{1}{2} \ln \sigma_g$. Here, D represents the diameter of particles (in micrometers), $\ln D_g$ is the geometric
 354 mean diameter, and $\ln \sigma_g$ is the geometric standard deviation (Lamb and Verlinde, 2011). The number of bioprotein aerosols
 355 was below the limit of detection in some samples, so that, only the curves of organics and dust were fitted. The fitting
 356 parameters of the same species were aggregated in parameter space, and were suspected to be related to the physical properties
 357 of each species, requiring further studies for confirmation. Moreover, the fitting parameters of organics and dust particles were
 358 clustered into two centroids (Fig. 10b) by the K-means method, which indicated that organics and dust have two classic modes
 359 (classic mode of organics: $\ln D_o = -0.70$, $\ln \sigma_o = 0.91$, and $N_o = 9.19 \times 10^5 \text{ cm}^{-3}$; classic mode of dust: $\ln D_d = 0.11$, $\ln \sigma_d$

360 = 1.07, and $N_o = 1.59 \times 10^6 \text{ cm}^{-3}$). That is, insoluble organics in hailstones are usually smaller in diameter and present in lower
 361 amounts than dust. Regardless of fine or coarse particles ($D < 0.5 \mu\text{m}$ in diameter were not considered in reference to DeMott
 362 et al. (DeMott et al., 2010)), the number concentration of dust was up to 2 orders of magnitude higher than the number
 363 concentration of organics. These observations indicated that dust accounted for the major portion of particles in eight
 364 hailstorms (no considering about bioprotein), which was consistent with the observations of embryos described above.



365
 366 **Fig. 10: Fitting size distribution functions of organics and dust contained in the whole hailstone. (a) Fitting parameters of logarithmic**
 367 **normal distributions of BJ1, BJ2, BS, FS, GY1, GY2, YT, GYA. (b) Classic modes of dust and organics (interval of data is $0.2 \mu\text{m}$)**

368 and fitting curves painted with interval of 0.02 μm). The fitting range of (a) is shown with a green rectangle. The centroid of the
369 organics fitting parameter (orange line) is $\ln \sigma_o = 0.91$, $\ln D_o = -0.70$, and $N_o = 9.19 \times 10^5 \text{ cm}^{-3}$. The centroid of the dust fitting
370 parameter (blue line) is $\ln \sigma_d = 1.07$, $\ln D_d = 0.11$, and $N_d = 1.59 \times 10^6 \text{ cm}^{-3}$. Shading showed uncertainty of organics and dust.
371 Abbreviations (corresponding to Table 1): BJ - BeiJing; BS - BaiSe; FS - FuShun; GY - GuYuan; GYA - GuiYAng; YT - YanTai.

372 4 Conclusions

373 This was the first study to simultaneously analyze both the number concentrations and species (including organics, dust
374 and bioproteins) of insoluble particles in hailstones. The findings from this analysis offer valuable insights into particle
375 observations within severe storms. Understanding the number concentration and composition of these insoluble particles is
376 crucial, as they play a significant role as ice-nucleating particles during the heterogeneous nucleation process in deep
377 convection.

378 The size distribution of insoluble particles in hailstones from the same hailstorm showed less variation than those from
379 different hailstorms. One possible reason is that updrafts of hailstorms brought insoluble particles from local surfaces or
380 boundary layers into deep convective clouds. Moreover, almost all insoluble particles in hailstone embryos analyzed in this
381 study showed an exponential size distribution, which was consistent with the effects of gravity. The number concentrations of
382 organics and dust from different hailstone embryos differed up to 389 times and 526 times at the same diameter, respectively.
383 The changes in particle concentration may lead to at least one-order-of-magnitude variance in ice-nucleating particle (DeMott
384 et al., 2010). Additionally, size distribution of insoluble particles varied in shells up to 27 times, which was much smaller than
385 differences with different hailstorms.

386 Two logarithmic normal distribution models were applied to fit the size distribution of organics and dust within hailstones,
387 providing a description of insoluble particles in the deep convection during hailstone formation. The analysis of the two classic
388 size distribution modes of insoluble particles indicated a significant presence of dust, without considering bioprotein.
389 Furthermore, a positive correlation exists between the number concentrations of insoluble particles and that of ice-nucleating
390 particles in hailstones, specifically for corresponding species (Ren et al., 2023, submitted, figure not shown). A further
391 measurement of ice-nucleating particles by drop-freezing experiments will establish the relationship between insoluble
392 particles and immersion ice-nucleating particles. Combination of these results with future experiments to determine the number
393 concentrations and species of particles from local observations will establish the relationship between surface observation and
394 ice-nucleating particles in deep convective clouds, which will lead to improvement of the parameterization of ice-nucleating
395 particles in both weather and climate models.

396 Nonetheless, two kinds of classic size distribution modes of organics and dust in hailstones were performed, but a more
397 robust classic mode required a larger number of samples. In future, for climate or weather models, the classic mode can be

398 assumed as the mean state to describe the characteristics of insoluble particles in supercooling water. In addition, this study
399 did not attempt to parameterize bioprotein aerosols, because there was a great uncertainty in quantification due to poor
400 understanding of biological processes (Fröhlich-Nowoisky et al., 2016). Further collaborative studies are required to gain a
401 better understanding of biological processes to establish the classic bioprotein mode.

402 **Code availability**

403 Self-organized maps algorithm is functions on MATLAB

404 <https://ww2.mathworks.cn/help/deeplearning/ref/selforgmap.html>

405 Random forest algorithm is functions on MATLAB

406 https://ww2.mathworks.cn/help/stats/treebagger.html?searchHighlight=TreeBagger&s_tid=srchtitle_TreeBagger_1

407 The 10-fold stratified cross-validation algorithm is functions on MATLAB

408 https://ww2.mathworks.cn/help/stats/cvpartition.html?searchHighlight=cvpartition&s_tid=srchtitle_cvpartition_1

409 Identification algorithms are coded on MATLAB and will be made available on request.

410 **Data availability**

411 Data will be made available on request.

412 **Author contributions**

413 Haifan Zhang wrote the original draft under the concept presented by Qinghong Zhang. Haifan Zhang, Xiangyu Lin and
414 Chan-Pang Ng participated in preprocess and reservation of hailstones from volunteers. Haifan Zhang and Xiangyu Lin sliced
415 hailstones using machine manufactured by Kai Bi and performed the experiments on analyzing element weight ratio of
416 insoluble particles with help of Li Chen. Kai Bi also provided hailstones BJ2 ~ BJ6. Machine learning on identification of
417 particles is operated by Haifan Zhang. Yangze Ren and Huiwen Xue compared ice nucleation particles from drop-freezing
418 experiments with our data. Zhuolin Chang provided hailstones GY1 and GY2. All authors discussed and contributed to the
419 final manuscript. Qinghong Zhang directed this project.

420 **Competing interests**

421 The authors declare no competing interests.

422

423 **Acknowledgments**

424 This study was supported by the National Natural Science Foundation of China (Grant Nos. 42030607 and 41930968),
425 the Innovation Project of the China Meteorological Administration (Grant No. CXFZ2021J038) and the Key R & D projects
426 in Ningxia Hui Autonomous Region (2022BEG02010). The authors thank Cai Yao from the Meteorological Bureau of
427 Guangxi, China in collecting hailstones BS in Guangxi. The authors thank volunteers in collecting hailstones. The authors
428 thank Prof. Jiwen Fan from Pacific Northwest National Laboratory of the United States for discussions.

429 **References:**

430 Aztec User Manual:

431 <https://utw10193.utweb.utexas.edu/InstrumentManuals/Oxford%20EDS%20AZtec%20User%20Manual.pdf>, last access:
432 22 August 2023.

433 Battaglia, A., Mroz, K., and Cecil, D.: Satellite hail detection, in: *Precipitation Science*, Elsevier, 257–286,

434 <https://doi.org/10.1016/B978-0-12-822973-6.00006-8>, 2022.

435 Beal, A., Martins, J. A., Rudke, A. P., de Almeida, D. S., da Silva, I., Sobrinho, O. M., de Fátima Andrade, M., Tarley, C. R.

436 T., and Martins, L. D.: Chemical characterization of PM_{2.5} from region highly impacted by hailstorms in South

437 America, *Environ. Sci. Pollut. Res.*, 29, 5840–5851, <https://doi.org/10.1007/s11356-021-15952-6>, 2022.

438 Calinski, T. and Harabasz, J.: A dendrite method for cluster analysis, *Commun. Stat. - Theory Methods*, 3, 1–27,

439 <https://doi.org/10.1080/03610927408827101>, 1974.

440 Chen, Q., Yin, Y., Jiang, H., Chu, Z., Xue, L., Shi, R., Zhang, X., and Chen, J.: The Roles of Mineral Dust as Cloud

441 Condensation Nuclei and Ice Nuclei During the Evolution of a Hail Storm, *J. Geophys. Res. Atmos.*, 124, 14262–

442 14284, <https://doi.org/10.1029/2019JD031403>, 2019.

443 Davies, D. L. and Bouldin, D. W.: A Cluster Separation Measure, *IEEE Trans. Pattern Anal. Mach. Intell.*, PAMI-1, 224–

444 227, <https://doi.org/10.1109/TPAMI.1979.4766909>, 1979.

445 DeMott, P. J., Prenni, A. J., Liu, X., Kreidenweis, S. M., Petters, M. D., Twohy, C. H., Richardson, M. S., Eidhammer, T.,

446 and Rogers, D. C.: Predicting global atmospheric ice nuclei distributions and their impacts on climate, *Proc. Natl. Acad.*

447 *Sci.*, 107, 11217–11222, <https://doi.org/10.1073/pnas.0910818107>, 2010.

448 DeMott, P. J., Prenni, A. J., McMeeking, G. R., Sullivan, R. C., Petters, M. D., Tobo, Y., Niemand, M., Möhler, O., Snider,

449 J. R., Wang, Z., and Kreidenweis, S. M.: Integrating laboratory and field data to quantify the immersion freezing ice

450 nucleation activity of mineral dust particles, *Atmos. Chem. Phys.*, 15, 393–409, <https://doi.org/10.5194/acp-15-393->

451 2015, 2015.

452 Fröhlich-Nowoisky, J., Kampf, C. J., Weber, B., Huffman, J. A., Pöhlker, C., Andreae, M. O., Lang-Yona, N., Burrows, S.

453 M., Gunthe, S. S., Elbert, W., Su, H., Hoor, P., Thines, E., Hoffmann, T., Després, V. R., and Pöschl, U.: Bioaerosols in

454 the Earth system: Climate, health, and ecosystem interactions, *Atmos. Res.*, 182, 346–376,

455 <https://doi.org/10.1016/j.atmosres.2016.07.018>, 2016.

456 Hersbach, H., Bell, B., Berrisford, P., Biavati, G., Horányi, A., Muñoz Sabater, J., Nicolas, J., Peubey, C., Radu, R., Rozum,

457 I., Schepers, D., Simmons, A., Soci, C., Dee, D., and Thépaut, J.-N.: ERA5 hourly data on single levels from 1959 to

458 present, Copernicus Clim. Chang. Serv. Clim. Data Store (CDS).[data set],

459 <https://doi.org/https://doi.org/10.24381/cds.adbb2d47>, 2018.

460 Hoose, C. and Möhler, O.: Heterogeneous ice nucleation on atmospheric aerosols: a review of results from laboratory
461 experiments, *Atmos. Chem. Phys.*, 12, 9817–9854, <https://doi.org/10.5194/acp-12-9817-2012>, 2012.

462 Knight, N. C.: The Climatology of Hailstone Embryos, *J. Appl. Meteorol.*, 20, 750–755, <https://doi.org/10.1175/1520->
463 0450(1981)020<0750:TCOHE>2.0.CO;2, 1981.

464 Kohonen, T.: The self-organizing map, *Proc. IEEE*, 78, 1464–1480, <https://doi.org/10.1109/5.58325>, 1990.

465 Lamb, D. and Verlinde, J.: *Physics and Chemistry of Clouds*, Cambridge University Press, Cambridge,
466 <https://doi.org/10.1017/CBO9780511976377>, 2011.

467 Li, X., Zhang, Q., Zhu, T., Li, Z., Lin, J., and Zou, T.: Water-soluble ions in hailstones in northern and southwestern China,
468 *Sci. Bull.*, 63, 1177–1179, <https://doi.org/10.1016/j.scib.2018.07.021>, 2018.

469 Li, X., Zhang, Q., Zhou, L., and An, Y.: Chemical composition of a hailstone: evidence for tracking hailstone trajectory in
470 deep convection, *Sci. Bull.*, 65, 1337–1339, <https://doi.org/10.1016/j.scib.2020.04.034>, 2020.

471 Michaud, A. B., Dore, J. E., Leslie, D., Lyons, W. B., Sands, D. C., and Priscu, J. C.: Biological ice nucleation initiates
472 hailstone formation, *J. Geophys. Res. Atmos.*, 119, 12,186-12,197, <https://doi.org/10.1002/2014JD022004>, 2014.

473 Prenni, A. J., Demott, P. J., Rogers, D. C., Kreidenweis, S. M., Mcfarquhar, G. M., Zhang, G., and Poellot, M. R.: Ice nuclei
474 characteristics from M-PACE and their relation to ice formation in clouds, *Tellus B*, 61, 436–448,
475 <https://doi.org/10.1111/j.1600-0889.2009.00415.x>, 2009.

476 Rogers, D. C., DeMott, P. J., Kreidenweis, S. M., and Chen, Y.: A Continuous-Flow Diffusion Chamber for Airborne
477 Measurements of Ice Nuclei, *J. Atmos. Ocean. Technol.*, 18, 725–741, <https://doi.org/10.1175/1520->
478 0426(2001)018<0725:ACFDCF>2.0.CO;2, 2001.

479 Rosinski, J.: Solid Water-Insoluble Particles in Hailstones and Their Geophysical Significance, *J. Appl. Meteorol.*, 5, 481–
480 492, [https://doi.org/10.1175/1520-0450\(1966\)005<0481:SWIPIH>2.0.CO;2](https://doi.org/10.1175/1520-0450(1966)005<0481:SWIPIH>2.0.CO;2), 1966.

481 Rousseeuw, P. J.: Silhouettes: A graphical aid to the interpretation and validation of cluster analysis, *J. Comput. Appl.*
482 *Math.*, 20, 53–65, [https://doi.org/10.1016/0377-0427\(87\)90125-7](https://doi.org/10.1016/0377-0427(87)90125-7), 1987.

483 Sibson, R. and Hartigan, J. A.: Clustering Algorithms., *Appl. Stat.*, 25, 70, <https://doi.org/10.2307/2346526>, 1976.

484 Tao, J., Zhang, L., Cao, J., and Zhang, R.: A review of current knowledge concerning PM_{2.5} chemical composition, aerosol
485 optical properties and their relationships across China, *Atmos. Chem. Phys.*, 17, 9485–9518,
486 <https://doi.org/10.5194/acp-17-9485-2017>, 2017.

487 Taylor, J. R.: *An Introduction to Error Analysis*, Second edi., University Science Books, 330 pp., 1997.

488 Vali, G.: *Ice Nucleation Relevant to Formation of Hail*, 1968.

489 Vergara-Temprado, J., Miltenberger, A. K., Furtado, K., Grosvenor, D. P., Shipway, B. J., Hill, A. A., Wilkinson, J. M.,
490 Field, P. R., Murray, B. J., and Carslaw, K. S.: Strong control of Southern Ocean cloud reflectivity by ice-nucleating

491 particles, Proc. Natl. Acad. Sci., 115, 2687–2692, <https://doi.org/10.1073/pnas.1721627115>, 2018.

492